Smart Materials and Structures

PURPOSE-LED PUBLISHING™

PAPER • **OPEN ACCESS**

Experimental investigation of the thermal history in FDM-based 4D printing

To cite this article: Philipp Herder *et al* 2026 *Smart Mater. Struct.* **35** 065039

IOP Publishing Smart Mater. Struct. 35 (2026) 065039 https://doi.org/10.1088/1361-665X/ae7686

Smart Materials and Structures

Check for updates

OPEN ACCESS

RECEIVED
23 January 2026

REVISED
3 May 2026

ACCEPTED FOR PUBLICATION
2 June 2026

PUBLISHED
23 June 2026

PAPER

Experimental investigation of the thermal history in FDM-based 4D printing

Philipp Herder[1,3], **Ferdinand Cerbe**[1,3,*], **Michael Sinapius**[1] and **Christian Hühne**[1,2]

[1] Institute of Mechanics and Adaptronics, TU Braunschweig, Langer Kamp 6, 38106 Braunschweig, Germany
[2] Institute of Lightweight Systems, German Aerospace Center (DLR), Lilienthalplatz 7, 38108 Braunschweig, Germany
[3] These authors contributed equally to this work.
[*] Author to whom any correspondence should be addressed.

E-mail: f.cerbe@tu-braunschweig.de

Keywords: 4D printing, shape memory polymers, thermal history, infrared (IR) thermography, residual stress gradient

Supplementary material for this article is available online

Abstract

Fused deposition modeling (FDM)-based 4D printing is a cost-efficient approach for manufacturing smart structures from thermoplastic filaments. During printing, pre-strain is stored in the deposited lines and later released during thermal activation, causing shape change. While printing parameters mainly influence shrinkage, even consistent process settings result in bending. This work investigates the thermal history during FDM-based 4D printing and its effect on layer-wise pre-strain and shape change. First, the influence of nozzle temperature, printing speed, part cooling fan, and build plate temperature on the cooling of a single printed line is quantified. Second, the thermal history of multilayer structures is examined using temperature and time metrics for the thermal event during deposition ($T_{\text{print,max}}$,$\Delta t_{\text{print},T>T_g}$) and overprinting ($T_{\text{reheat,max}}$,$\Delta t_{\text{reheat},T>T_g}$). Finally, the multilayer structures are thermally activated, and the shape change is characterized using shrinkage and curvature, which indicate the pre-strain and its gradient across the specimen height. The multilayer structures shrink and bend. The curvature direction indicates higher pre-strain in the bottom layers. Thermal history metrics increase towards higher layers, indicating more relaxation, which reduces pre-strain in the top layers. This indicates that the thermal history has a decisive role in pre-strain formation. The reduction of the nozzle temperature by 30° C causes a shrinkage increase of 8%–10% and a curvature increase of 25–30 m^{-1}. Notably, activating the part cooling fan causes a shrinkage increase of 1%–2% and a curvature decrease of 2–5 m^{-1}, which is consistent with smaller changes in thermal history metrics. Furthermore, this study indicates that the relaxation strongly depends on variations in printer design, process parameters, or material. Consequently, modifications that alter the polymer melt's flow, heat transfer, thermal capacity, or viscoelastic relaxation affect the shrinkage and curvature.

1. Introduction

4D printing extends **additive manufacturing (AM)** by enabling the fabrication of smart structures that change their shape or functional properties over time in response to external stimuli [1]. By utilizing smart materials in AM, technology has evolved from static structural parts to dynamic smart structures. The dynamic smart structure undergoes a programmed transformation when exposed to a specific stimulus, typically an environmental change [2] or an intentionally applied field [3], whose nature depends on the underlying material system. Reported stimuli include temperature [4, 5], light [6, 7], ultraviolet radiation [8], **infrared radiation (IR)** [9], moisture [1, 10, 11], magnetic fields [12] and electric fields [13]. These activation mechanisms enable applications across healthcare, aerospace, soft robotics, electronics, photonics, and the construction industry [14]. To support such applications, various AM techniques have been adapted for smart materials, including material extrusion [15], vat photopolymerization [16], powder bed fusion [17, 18], binder jetting [19], and material jetting [1, 20,

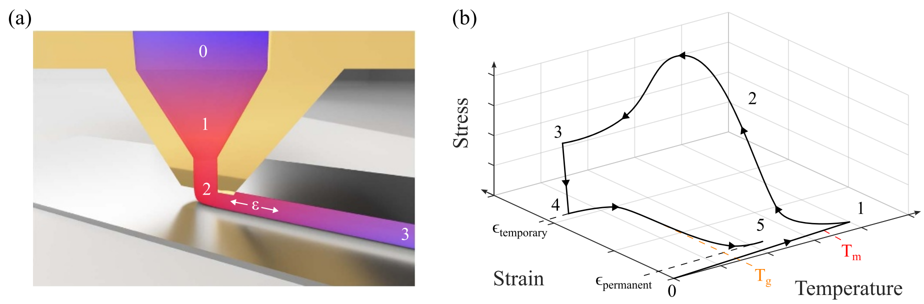

Figure 1. The FDM-based 4D printing process (a) relates to the shape-memory cycle (b) [28]. (a) and (b) Reproduced from [28].

21]. Despite rapid progress over the past decade, key challenges remain in improving the precision, repeatability, and controllability of smart structures, as well as in developing predictive mathematical and theoretical models to explain the physical mechanism, reducing experimental efforts [14, 22].

Fused deposition modeling (FDM) has emerged as a promising process for 4D printing because it supports a broad range of thermoplastic and composite materials, is straightforward to operate and modify, and remains a low-cost AM technology [14]. Nevertheless, FDM also presents notable limitations for smart-material fabrication, including relatively low resolution, diversity across printer designs, and the fact that most commercially available systems were originally developed for producing static components rather than stimuli-responsive structures. Despite these constraints, the accessibility and affordability of consumer-grade FDM systems make them the most widely adopted technology for experimental 4D printing [14]. Ongoing developments specifically design shape memory polymers for 4D printing [23–26], but commercially available **Polylactic acid (PLA)** has been shown to be a cost-efficient material for creating smart structures using FDM-based 4D printing [27]. Although PLA is not a common smart material, its temperature-sensitivity qualifies it as a smart material in a broader sense. The printing process creates the temporary shape, but printing parameters can be used to program a pre-strain, ultimately controlling a shape change upon reheating [27]. However, these process dependencies are complex, underscoring the need for generalizable investigations of the physical quantities.

FDM-based 4D printing is similar to the programming step in the thermo-responsive shape-memory cycle [15, 29–32], as illustrated in figure 1. During printing, the cold filament (0) is fed into the nozzle, where it is heated (1). The material is then extruded and deposited onto the build plate, where the material experiences shear and elongational flows that orient the polymer chains, leading to a pre-strain in the printed line (2). After deposition, it rapidly cools and solidifies (3). This rapid cooling fixes this non-equilibrium conformation by reducing the molecular mobility below its transition temperature, thereby storing the pre-strain within the molecular structure. When removing the part from the build plate, the smart structure remains in its temporary shape (4). Reheating it above its transition temperature (5) causes shape transformation from the temporary to the permanent shape.

The fundamental difference between FDM-based 3D printing and 4D printing lies in the process control. In standard 3D printing, the pre-strain is minimized because the extruded material cools relatively slowly, allowing molecular relaxation toward the equilibrium state. As a result, the printed part exhibits little or no shape change when reheated. In contrast, 4D printing intentionally seeks to retain a controlled level of pre-strain. This requires a reproducible non-equilibrium state generated during extrusion and deposition, and suppressing relaxation during cooling. These opposing process objectives demonstrate that temperature-dependent relaxation has a decisive influence on the stored pre-strain, underscoring the central importance of the material's temperature history.

Printing parameters are widely recognized as the primary factors influencing the amount of pre-strain [4]. However, even when identical settings are used for the entire print, the resulting shape change indicates a pre-strain gradient across layers. This gradient arises from variations in deposition conditions that affect cooling rates and reheating of each deposited line, thereby creating a location-dependent thermal history. Bodaghi *et al* identify several parameters that shape this thermal history, including the build plate temperature, material and surface roughness, the printing speed, nozzle temperature, and interlayer delay time [15]. Several studies have reported that upper layers store more pre-strain [15, 29, 30, 33–35], attributing this to greater relaxation in the lower layers due to reheating during subsequent deposition. In contrast, other researchers have found higher pre-strain in the lower layers [32, 36],. Their results suggest that lower layers cool faster and transfer heat more effectively to the build plate, thereby suppressing relaxation and increasing pre-strain. Despite the different results, all studies point to the decisive role of the thermal history. Consequently, characterizing the thermal history is promising to control pre-strain.

Although thermal history is a process-level indicator of the layer-wise inhomogeneity, the physical mechanism is the temperature-dependent relaxation of the polymer. Relaxation originates from molecular mobility, where macromolecules gradually rearrange toward their equilibrium through mechanisms such as segmental motion and reptation [37, 38]. Classical viscoelastic models, such as Maxwell and Kelvin–Voigt models, capture relaxation and creep but remain simplified. Because relaxation accelerates strongly with temperature, Williams, Landel, and Ferry (WLF) established the time-temperature superposition principle and the associated WLF equation. In this relationship, the relaxation time significantly decreases as the temperature exceeds the glass transition temperature [39]. Direct measurement of relaxation during printing is difficult due to the process dynamics and repeated reheating of deposited layers. Consequently, monitoring the thermal history provides a practical indirect method to investigate relaxation differences and improve our understanding of pre-strain storage.

Previous studies investigated the thermal history during FDM printing, primarily focusing on the quality of 3D-printed parts [40–44]. However, the experimental and numerical focus has not been on the pre-strain, which is relevant for 4D printing. Therefore, these insights provide the theoretical foundation for our study.

The line-based nature of FDM creates three distinct thermal scenarios: (i) cooling of a line immediately after extrusion, (ii) reheating of adjacent lines within the same layer, and (iii) reheating of previously deposited underlying layers. The cooling behavior of an extruded line typically follows an exponential decay, starting at a peak temperature near the nozzle temperature and approaching either the build plate or ambient temperature over time [40, 41, 44–48]. Reheating of adjacent lines primarily raises the temperature in the contact region between them, after which both lines cool together [49]. Similarly, deposition of a new layer reheats the underlying layer, causing a temporary temperature rise and subsequent joint cooling of the two layers [41, 45–48].

IR thermography is a contact-free alternative to embedded sensors, avoiding process disruptions, flow alterations, and added thermal mass. Instead, it determines surface temperature by detecting thermal radiation [50]. IR imaging provides continuous spatial and temporal temperature fields and has therefore proven valuable for process monitoring [40, 48, 49]. However, it is limited to the object's surface temperature and cannot detect its internal temperature. Depending on the camera orientation, IR thermography has been used to investigate interlayer bonding from side-view configurations [40, 48] and adjacent-line interactions from bottom-view setups [49], offering intra- and inter-layer perspectives on thermal behavior. Overall, IR thermography is an effective method for capturing the spatial and temporal temperature evolution during FDM printing, yet it has not been applied in the 4D printing process.

The main objective of this work is to provide a systematic link between a structure's thermal history, stress relaxation, and pre-strain, through an experimental investigation of process and shape change. The author's previous study found that the relationship between printing forces and shape change is not unique, indicating the relevance of the thermal history [32]. In the process, the printing force in the x-direction is measured using a force sensor below the build plate. Additionally, the temperature is measured using IR thermography. The thermal history and its key characteristics suggest differences in stress relaxation across the print. The shape change upon thermal activation is an indicator of the pre-strain. Although pre-strain gradients have been previously attributed to differences in thermal history and consequent relaxation, empirical evidence has been lacking. Therefore, this study provides valuable contributions in three sections:

1. cooling behavior of single extruded lines (section 3.1),
2. cooling and reheating dynamics in multi-layer 4D structures (section 3.2), and
3. the resulting shape changes of multilayer 4D structures (section 3.3).

2. Materials and methods

This experimental study focuses on two experiments. In the first experiment, the cooling behavior of a single line was characterized. Four parameters were varied on three levels to determine their influence on single-line cooling. In the second experiment, the temperature and printing force were measured during printing multilayer structures. Indicators were defined to characterize the thermal history, focusing on

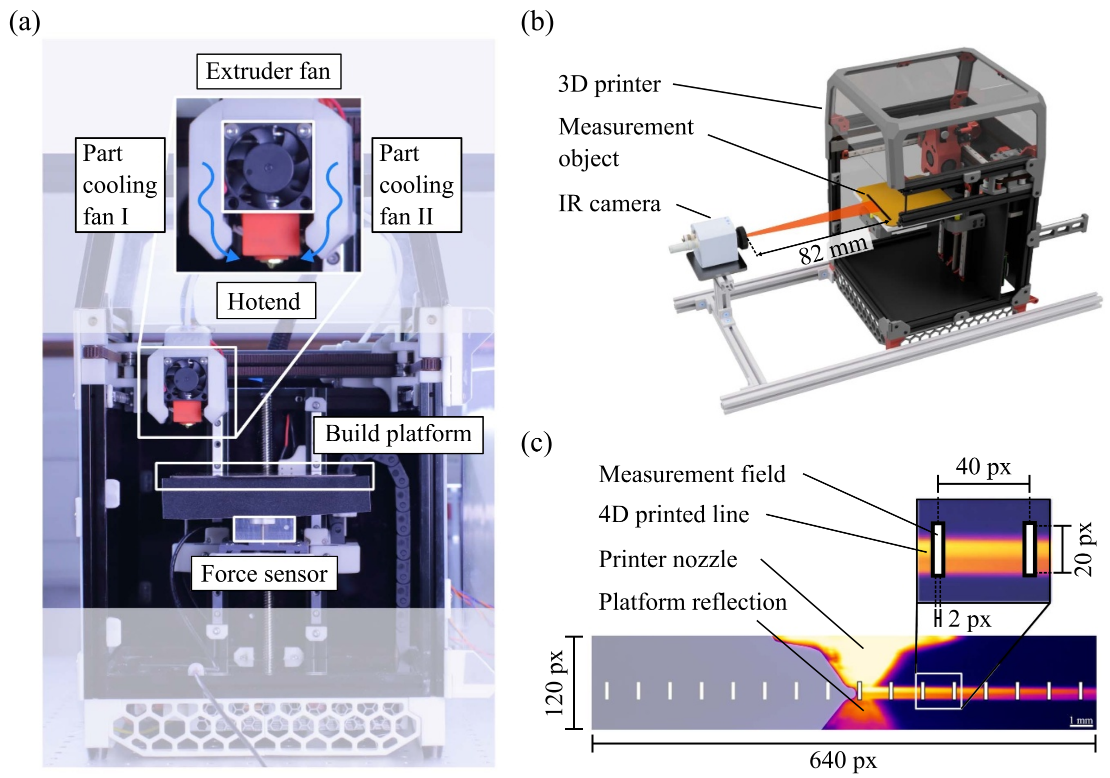

Figure 2. Printing setup with a detailed view of the printing head and a force sensor mounted underneath the build plate (a). Side-view positioning of the IR camera in front of the printer (b) allows for filming the printing of a line horizontally (c). The total width of the IR image spans a horizontal distance of 22 mm (1 px = 0.0344 mm). (a)–(c) Reproduced from [28]. CC BY 4.0.

two thermal events, cooling and reheating. These multilayer structures were activated, and the stimulus-induced shape change was quantified. The thermal history, printing forces, and shape change were then used to discuss stress relaxation during the manufacturing process of 4D structures.

2.1. Experimental equipment

In this investigation, a Voron V0.1 3D printer configured in a CoreXY arrangement, equipped with a bowden extruder, an e3Dv6 hotend, and a 0.4 mm nozzle, was used. The printer head has three fans. The extruder fan cools the hotend, the two part-cooling fans direct airflow towards the printed part, see figure 2(a). The g-code for all specimens in this investigation was prepared with *PrusaSlicer*. To measure printing force, the build plate was mounted on a three-axis force sensor (K3D40 10 N, ME-Messsysteme, Germany) with a nominal load capacity of ± 10 N and an accuracy class of 0.5, representing a compromise between robustness and sensitivity. The sensor output was processed via a GSV-8DS SubD44HD measurement amplifier (ME-Messsysteme, Germany) and recorded using the *GSVmultiChannel* software at a sampling rate of 200 Hz. To minimize external disturbances, the entire setup was placed on a vibration-isolated table.

The temperature monitoring was carried out using an IR camera (TIM 640 VGA, Micro-Epsilon, Germany) equipped with a microbolometer detector. The camera was positioned in a side-view in front of the 3D printer, as seen in figure 2(b). Note that the IR measurement is limited to surface temperatures only, but does not capture internal temperatures. The optical setup consisted of a microscope lens with a focal length of 44 mm, providing a field of view of 12° × 9°. Thermal radiation in the spectral range of 7.5–13 μm was detected by the IR camera operating at a frame rate of 125 Hz. The recording was conducted in partial image mode with a spatial resolution of 640 × 120 px (full-frame resolution: 640 × 480 pixels), while the temperature measurement range was set to 0° C–250° C. The system accuracy is specified by the manufacturer as ± 2° C or ± 2% of the measured value, whichever is greater. Camera configuration, video recording, measurement field positioning, and subsequent video evaluation were handled using the *thermoIMAGER TIM Connect* software. The image scale was calibrated using a metal ruler, see figure 2(c), resulting in a distance-to-pixel ratio of 0.0344 mm/px. The printing direction was perpendicular to the camera's line of sight, so that both the printed line and the first line of a layer for the multilayer structure crossed the image horizontally from right to left.

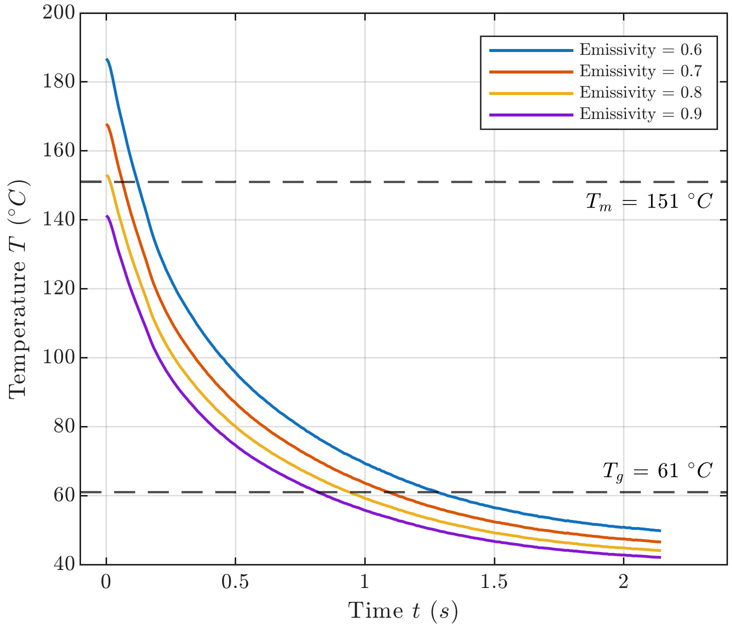

Figure 3. The emissivity is varied for the analysis of the IR measurement (specimen 9 of series TN210-TB30-V50-B0). Decreasing emissivity increases the calculated temperature. The emissivity was calibrated using reference measurements with a thermocouple for T_n = 190, 210, and 230° C. The results are shown in table 1.

Table 1. Emissivity of the PLA melt, calibrated for the experimental setup.

Set temperature T_n (Slicer)	Nozzle tip temperature (actual)	Effective emissivity
190 °C	159.9 °C	0.649
210 °C	175 °C	0.676
230 °C	194 °C	0.696

Table 2. Properties of BASF Ultrafuse PLA filament.

Material properties	Value	Standard
Glass transition temperature T_g	61 °C / 142 °F	ISO 11 357−3
Melting temperature T_m	151 °C / 304 °F	ISO 11357−3
Density ρ	1248 kg m^{-3}	ISO 1183−1
Melt volume flow rate $\dot{V}$	2.12 cm^3 min^{-1}	ISO 1133

IR temperature measurements are sensitive to the emissivity of the object being measured, because it defines the conversion of thermal radiation into temperature, see figure 3. The emissivity of an object primarily depends on its material properties and surface characteristics. In theory, PLA has an emissivity of approximately 0.9, which is typical for many plastics [51–53]. However, in this study, the object of interest was the molten filament immediately after extrusion. Its smooth, glossy surface reduced the effective emissivity. Therefore, emissivity was determined by measuring the temperature at the nozzle tip with a type-K thermocouple. This approach was used by Ferraris *et al* who determined an emissivity of 0.78 at a material temperature of 60.4 °C [45].

The underlying assumption to calibrate the emissivity was that the measured temperature at the nozzle tip corresponded to the temperature of the filament as it exits the nozzle. The emissivity setting of the IR camera was then adjusted to match the IR-measured material temperature to the thermocouple-measured nozzle-tip temperature. This was carried out for three different nozzle temperatures between 190 °C and 230 °C (table 1), which covered the range of the nozzle temperature used in the experiments. The effective emissivity was set to 0.675 and kept constant for the investigation.

2.2. Material

In this research, Ultrafuse PLA filament (BASF, Germany) (T_g = 61 °C) with a diameter of 1.75 mm was used. Table 2 represents an extract of the material properties from the datasheet.

Table 3. Printing parameters for single-line experiments.

Printing parameter	Value
Nozzle temperature T_n	190, 210, 230 °C
Build plate temperature T_b	30, 40 °C
Print speed v_p	20, 50, 80 mm s^{-1}
Fan speed B	0, 50, 100%
Layer height h_L	0.2 mm
Extrusion width w_L	0.45 mm
Example parameter-set	TN190-TB30-V20-B0

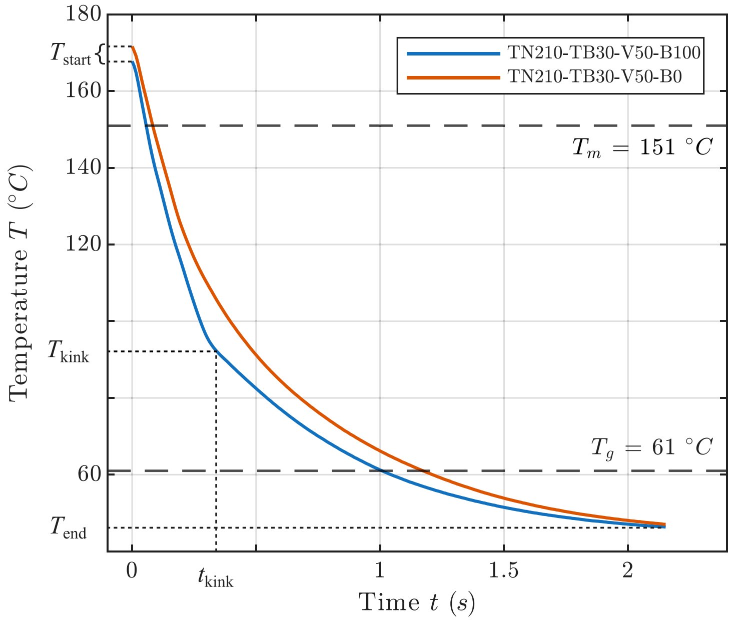

Figure 4. Cooling curves of specimens printed with the cooling fan at 100% (B100) and with the fan off (B0) recorded at a frame rate of 125 Hz. With the fan off, the curve shows a smooth decay and a higher starting temperature. With the fan on, the curve exhibits a distinct kink after 0.31 s (equivalent to 15.5 mm from the nozzle), which divides the curve into two regions. In this case, the starting temperature T_{start} is lower.

2.3. Method for parameter-dependent cooling

The first experiment focused on the parameter-dependent cooling of a single line. The single-line specimen had the dimensions: 80 × 0.45 × 0.2 mm^3 (w × d × h). Before each specimen, a prime line was printed to create a quasi-static extrusion. Four printing parameters were varied: nozzle temperature T_n, build plate temperature T_b, printing speed v_p and part cooling fan speed B. The influence of the printing parameters on the cooling behavior was investigated in a full factorial experimental design. The design was chosen to avoid confounding effects from printing parameters and to determine interactions. The experimental design resulted in 54 specimen series, with each series printed 10 times, allowing for statistical evaluation. The levels of the printing parameters are shown in table 3.

Temperature measurement setup. The temperature of a single printed line was recorded using 16 digital measurement fields, every 2 × 20 pixels in size. The measurement fields were arranged horizontally along the printed line, see figure 2(c). For each measurement field, the maximum temperature over time was recorded. The 16 cooling curves were shifted in time to align. This is based on the observation that the 16 measurement fields record the same cooling curve. By calculating the arithmetic mean, the cooling of a specimen is determined. Each series contains 10 specimens, combined into a single cooling curve per series. In summary, the average cooling curve of a single specimen was derived from 16 spatially distributed measurement fields, and the average cooling curve of a series was obtained from 10 specimens.

Characterization and curve fitting. The resulting cooling curve was characterized by four points, see figure 4. T_{start} is the maximum recorded temperature directly after extrusion. T_{end} is the temperature recorded 2.15 s after extrusion but is inequal to the asymptotic temperature T_∞. This value was selected to ensure a consistent time window within the quasi-exponential cooling regime while avoiding late-stage measurement errors from the nozzle passing behind the printed line. Furthermore, each deposited line is

Table 4. Printing parameters for multi-layer 4D structures.

Printing parameter	Value
Nozzle temperature T_n	200, 230 °C
Build plate temperature T_b	40 °C
Print speed v_p	50, 80 mm s^{-1}
Fan speed B	0, 100%
Layer height h_L	0.2 mm
Extrusion width w_L	0.45 mm
Example parameter-set	TN200-TB40-V50-B0

reheated by adjacent or overlying lines, making T_∞ a theoretical value rather than a practically attainable condition in multilayer structures. All specimen series with an activated cooling fan showed a kink in the cooling curve, see figure 4. By calculating the maximum of the second derivative, the kink was located. T_{kink} and t_{kink} are the temperature and time of the kink, respectively. This kink resulted from the fan's design, which provided effective cooling within approximately 15 mm of the nozzle. Beyond this range, the increased cooling effect disappeared.

The cooling behavior was modeled using a first-order exponential decay function (equation (1)). The model assumes spatially uniform temperature, constant effective thermal properties, and convective cooling to a constant ambient temperature. Radiative effects were neglected. Santos *et al* used a similar analytical approach, but with Euler's number as the exponential basis [54]. Although their decay term used Euler's number (e) as the basis, it is interconvertible with our decay factor β. The model is valid only over time intervals with approximately constant cooling conditions. Therefore, for active cooling (B100, B50), only the fan-influenced region was fitted until t_{kink}, whereas for inactive cooling (B0), the entire cooling curve was used. Characterizing the cooling curve simplified the effect of printing parameters on the cooling curve and enabled a quantitative comparison of different printing conditions.

$$T(t) = T_{\text{end}} + (T_{\text{start}} - T_{\text{end}})\,\beta^{t}. \tag{1}$$

2.4. Method for parameter-dependent thermal history

The second experiment focused on the thermal history of a multilayer structure. The multilayer 4D structure consists of 6 layers and has the dimensions of: 40 $\times$ 15 $\times$ 1.2 mm^{-3} ($w \times d \times h$). The layers were printed in the x-direction, starting each layer in the front right corner of the build plate.

Before each print, the build plate was automatically mapped, using the nozzle as a tactile probe for consistent distance between them (*Klipper: BED MESH CALIBRATE*). Each print started with three skirts to ensure quasi-static extrusion conditions. This routine was observed to reduce variation, thereby improving data quality.

Due to the higher experimental effort for multilayer structures, a reduced DOE was applied, focusing on nozzle temperature T_n, printing speed v_p, and part cooling fan speed B (2 levels each, 8 combinations). The build plate temperature T_b, layer height h_L, and extrusion width w_L were kept constant. The lowest printing speed was omitted due to its limited practical relevance. Nozzle temperature levels were slightly adjusted to ensure stable processing of multilayer structures. The highest nozzle temperature was maintained for comparison (230 ° C). Each parameter set was printed 10 times in randomized order. The parameter variations are summarized in table 4.

Temperature measurement setup. The temperature of a multilayer structure was recorded at three measurement points on the camera-facing side of each layer, forming a 3 $\times$ 6 grid. The measurement point was 1 $\times$ 1 px, ensuring that layer temperature was measured, rather than the bonding region between layers. The three measurement points per layer allowed a statistical assurance of the measured temperature for each row of the grid.

The setup measured the 18 Temperatures continuously, but the focus was on the newly extruded and the overprinted line, see figure 5(a). Immediately after deposition ($t = t_0$), heat conduction started to transfer heat to colder areas, resulting in a temperature gradient at the time t_1, as shown in figure 5(b). Simultaneously, convective heat transfer from the ambient air caused the part to cool. The convective heat transfer causes the line to approach near-ambient temperature at the time t_2.

The raw data needed segmentation due to the CoreXY printer design. The position of the IR camera remained stable while the build plate lowered as the layers increased. After a layer change, the measurement continued in the subsequent row of the measurement grid. The first row of the measurement grid always recorded the cooling of the newly printed line. Segmentation and rearrangement of the data were

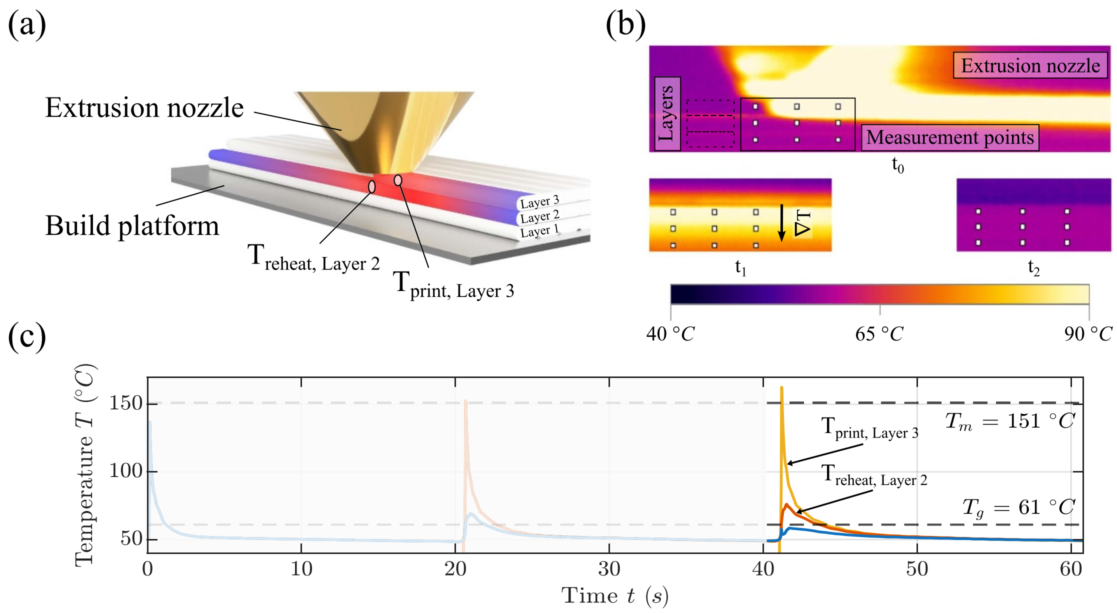

Figure 5. Visualization of the extrusion process of layer 3 (a). IR measurement of a multilayer object. The deposited material introduces heat into the object, which is transferred to the underlying layers and the environment until the object reaches equilibrium with its environment (b). Temperature curve of the layers extracted from the measurement points with an interlayer time $\Delta\, t_{\text{inter}}$ of 20.58 s (c).

based on the temperature peaks during deposition. Print head movements behind the first line resulted in smaller peaks in the cooling curve. These measurement errors were filtered in post-processing. The measurement grid provided three temperature curves per layer, which were averaged to one temperature curve per layer for each specimen. The layer temperatures of 10 specimens were averaged to one temperature curve per series.

The thermal history was characterized by four indicators that were determined from the newly printed layer T_{print} and the reheated layer T_{reheat}, see figure 5(c). $T_{\text{print,max}}$ was the maximum Temperature of T_{print}. $\Delta t_{\text{print},T>T_g}$ was defined by the time interval from the time of maximum temperature until T_{print} decreased below T_g. $T_{\text{reheat,max}}$ was the maximum temperature of T_{reheat}. $\Delta t_{\text{reheat},T>T_g}$ was the time interval from the time where T_{reheat} exceeded T_g until it cooled below.

The temperature measurement should provide insight into the premature relaxation of process-induced stresses when printing subsequent layers on top and reheating the underlying layer. Therefore, not only the maximum temperature but also the duration above the glass transition are relevant.

Signal processing for force measurements. A low-pass filter with a passband frequency of 15 Hz was applied to reduce noise and vibrations in the raw force signal caused by the printer's fans and motors. Negative spikes of the force signal in the *z*-direction marked the layer change, due to the inertia of the build plate. A change of sign of the signal in the printing direction marked the start and end points of a line. To calculate the printing force for a single line, the mean value of the inner 80% was taken, ensuring that acceleration-induced spikes at the beginning and end of each line were excluded. Force data processing resulted in a singular mean force $\bar{F}$ for each line. First, the force was determined for each line and subsequently averaged over all lines and layers to obtain the mean programming force of the entire structure.

2.5. Activation setup and shape measurement

After printing the multilayer structures, the samples were clamped in a fixture and immersed in a beaker filled with glycerol for 10 min. The beaker was placed in a water bath of a thermostat (F12-MA from JULABO GmbH, Germany), which maintained the glycerol at 90 °C. This experimental setup kept the glycerol temperature in the beaker constant, eliminating disturbances from the water circulation. The activation parameters are shown in table 5.

The initial length of the central fiber l_0 was measured to verify printing accuracy. After activation, the specimens were photographed and analyzed in *Fusion360*. Images were acquired with a fixed, perpendicular camera setup using a planar macro lens (ZEISS Milvus 100 mm). The specimen and reference scale were positioned in the same plane to minimize perspective and distortion effects. The resulting

Table 5. Activation parameters.

Parameter	Value
Activation medium	Glycerol 99.8 % PF
Glycerol density	1.263 – 1.265 $g\,cm^{-3}$
Activation temperature	90° C
Exposure time / dwell time	10 min

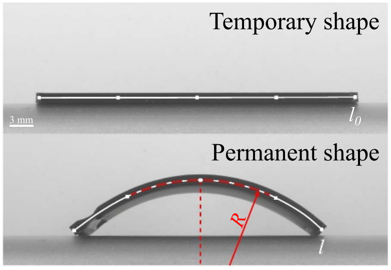

Figure 6. Thermal activation causes the 4D structure to change shape. The specimen shrinks along the central fiber and bends towards the build plate. The optical measurement points are placed on the central fiber to quantify the shape regarding length (l, l_0) and bending radius R.

measurement uncertainty is estimated to be on the order of $\pm$ 0.1 mm. For each specimen, the length of the central fiber l in the permanent shape was measured using a five-point spline fit, as illustrated in figure 6. Additionally, the specimen showed a bending response, with consistent curvature in the specimen's center. However, curvature changed towards the edges, which can be attributed to acceleration and deceleration during printing and clamping during activation. Therefore, a partial circle, optically measuring the radius R, was placed in the center section with consistent curvature.

The shrinkage strain was calculated by using the length of the central fiber of the structure before (l_0) and after (l) the activation, see equation (2).

$$\epsilon = \frac{l_0 - l}{l_0}. \tag{2}$$

The curvature was calculated from the optical measured radius R (equation (3)).

$$\kappa = \frac{1}{R}. \tag{3}$$

3. Results and discussion

Printing parameters affect the thermal history and the pre-strain in a 4D structure. Here, both their influence on the temperature evolution and on the resulting shape change are analyzed, and the experimental observations are discussed considering the underlying physical mechanisms. Therefore, the parameter-dependent cooling of a 4D line (section 3.1), the thermal history of a 4D structure (section 3.2), and the resulting shape change of a 4D structure (section 3.3) are presented in three subsections.

3.1. Parameter-dependent cooling of a 4D line

A single printed line does not form a complete 4D structure, but it is its smallest element and drives the shape change. The thermal evolution is quantified using equation (1) to characterize the cooling curve, which leads to the characteristics defined in section 2.3 (T_{start}, β, and T_{end}). The printing parameters are varied to determine the main dependencies:

$$T_{\text{start}} = f(?) \qquad \beta = f(?) \qquad T_{\text{end}} = f(?)$$

3.1.1. Start temperature T_{start}

The starting temperature T_{start} is primarily determined by the nozzle temperature T_n, with secondary influences from the printing speed v_p and the part cooling fan speed B, while the build plate temperature T_b has no significant effect (see figure 7 and table S2).

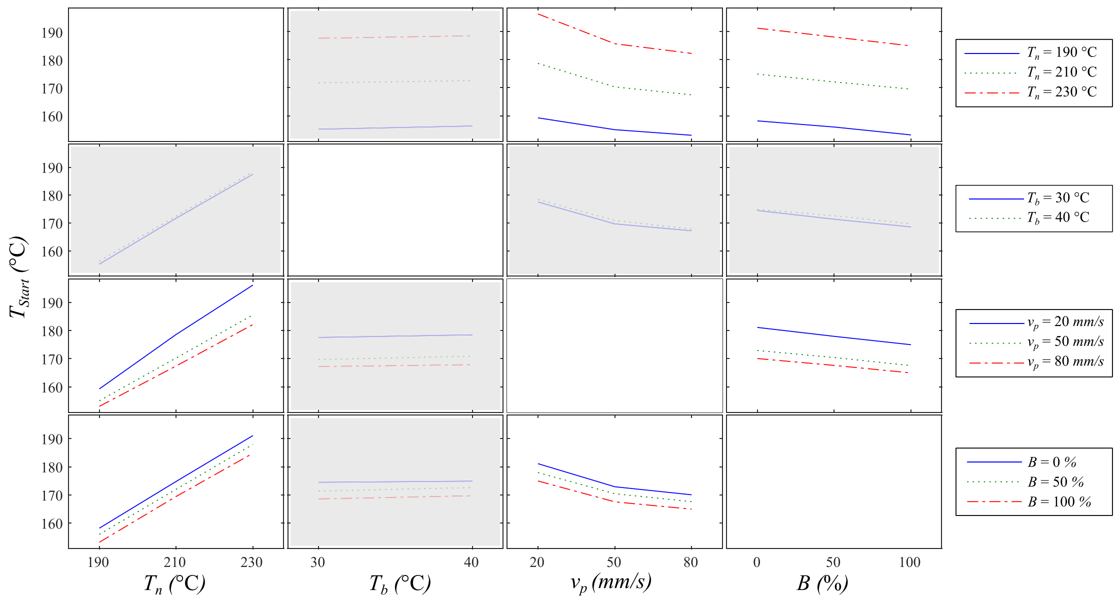

Figure 7. The printing parameter T_n is the dominant factor influencing the start temperature T_{start}. The printing speed v_p and fan speed B have a minor effect on T_{start}, while the influence of the build plate temperature T_b is negligible.

T_{start} has a linear relationship with T_n. Increasing the nozzle temperature setpoint causes the control system to supply more power to the embedded heater cartridge, increasing the thermal energy transferred to the filament and resulting in a higher recorded T_{start}.

Increasing v_p leads to a nonlinear decrease in T_{start}, with the largest effect observed at low v_p values. This behavior is attributed to the time-dependent heat transfer between the hotend and the filament. At higher material flow rates, the residence time of the filament within the hotend decreases, reducing the thermal energy transferred to the filament. Additionally, the increased material throughput acts as a heat sink. As a result, heat is removed from the nozzle, thereby also reducing T_{start}.

The part cooling fan speed B is inversely proportional to T_{start}, although its effect is minor compared to that of the nozzle temperature T_n. This behavior is due to the fan design, which directs airflow towards the nozzle from both sides and enhances convective heat dissipation. The heater cartridge acts as a localized heat source, while heat is simultaneously dissipated to the surroundings. Higher part cooling fan speeds B increase convective cooling of the nozzle tip, resulting in a lower T_{start}.

The limitations of the experimental setup must be considered, such as measurement accuracy ($\pm$ 2° C or $\pm$ 2%) and frequency (125 Hz). Printing parameters with only a minor influence on T_{start}, such as the part cooling fan speed B, are affected by the accuracy because the measured differences are small. Nevertheless, the influence of B is significant. The measurement frequency cannot capture thermal events shorter than 0.016 s, limiting the evaluation of v_p. To counter this measurement error, the 16 measurement fields were used and averaged within a print. Consequently, T_n, v_p, and B show significant effects on T_{start} (table S2).

3.1.2. Cooling factor β

The cooling factor β is primarily affected by the fan speed B, while no significant influence of the nozzle temperature T_n and the build plate temperature T_b was observed. The printing speed v_p affects β only when the fan is active.

Increasing the part cooling fan speed B leads to a decrease in the cooling factor β, across all printing speeds v_p (figure 8). Primarily, the fan increases convective heat transfer and thus accelerates cooling. Secondarily, increased heat conduction from the line's core to the surface is implied by a colder surface temperature, creating a steeper internal temperature gradient. Although the part cooling fan is effective in improving cooling, its effect is spatially limited to a nozzle distance of 15 mm.

A decrease in β with higher printing speed v_p is observed only when the part cooling fan is active, which is shown in the interaction plot in the supplementary material figure S2. At higher v_p, the smaller temperature drop $T_{start} - T_{kink}$ results in smaller fitted values of β. When the part cooling fan is activated, β is fitted only up to the kink time t_{kink}. With higher v_p, the time domain shifts from about 0.75 s at 20 mm s^{-1} to 0.19 s at 80 mm s^{-1}. Therefore, the effect of v_p remains uncertain.

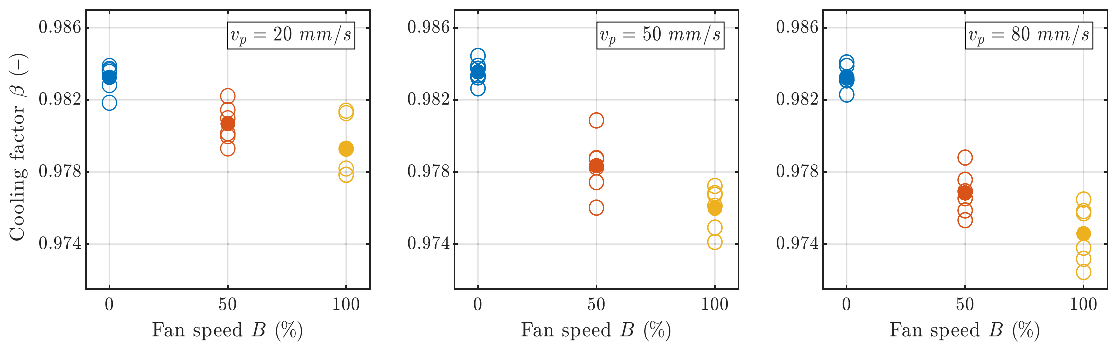

Figure 8. Influence of the part cooling fan speed B on the cooling factor β for different printing speed sv_p. The mean value of β consistently decreases with increasing fan speed B across all investigated print velocities v_p.

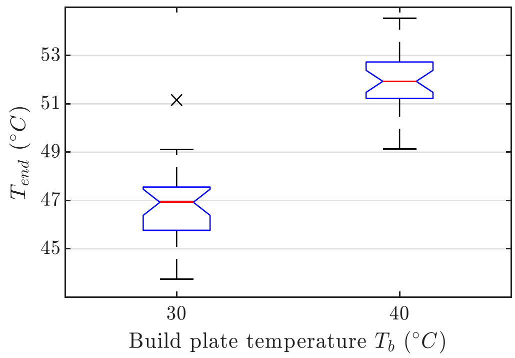

Figure 9. Boxplot illustrating the influence of the build plate temperature T_b on the final measured temperature T_{end}. T_{end} represents the temperature measured 2.15 s after extrusion. The results indicate a positive relationship, where T_{end} increases with increasing T_b. The notch on each boxplot visualizes the 95% confidence interval for the median.

Although the ANOVA in table S3 proposes significant effects of B and v_p, the shifted time domain for v_p reduces the reliability of the term. In summary, B is the significant and physically explainable parameter influencing β.

3.1.3. End temperature T_{end}

The end temperature T_{end} is primarily influenced by the build plate temperature T_b. Nozzle temperature T_n and part cooling fan speed B only exert small effects (see table S4). No significant influence of the printing speed v_p was observed.

Figure 9 shows that T_{end} increases with increasing build plate temperature T_b, based on the comparison of median plateau values. The notches in the boxplots indicate the 95% confidence intervals for the medians. The non-overlapping intervals demonstrate a significant influence of T_b on T_{end}. This proportional relationship is expected, as the build plate is in direct thermal contact with the printed line.

The effects of T_n and B are comparatively minor, as shown in the Supplementary material in figure S3 and table S4. Increasing the nozzle temperature leads to hotter extrusion and retains thermal energy for a longer duration, resulting in a slightly higher T_{end}. Conversely, increasing the part cooling fan speed B slightly reduces T_{end} by enhancing convective cooling.

Although the effects of T_n and B are considered significant in the ANOVA (table S4), their significance is limited by the IR camera's accuracy ($\pm$ 2° C). The effect of T_n on T_{end} is greater than the accuracy limitation, supporting its relevance. The effect of B on T_{end} is equal to the accuracy limitation, reducing its relevance. Therefore, the main influencing factor on T_{end} is T_b, with small but significant effects of T_n.

In summary, the parameters of equation (1) are influenced by the printing settings, with the main dependencies outlined below. The corresponding main-effect plot of the printing parameters on the characteristics is presented in the Supplementary material, see figure S1. Also, the data for the

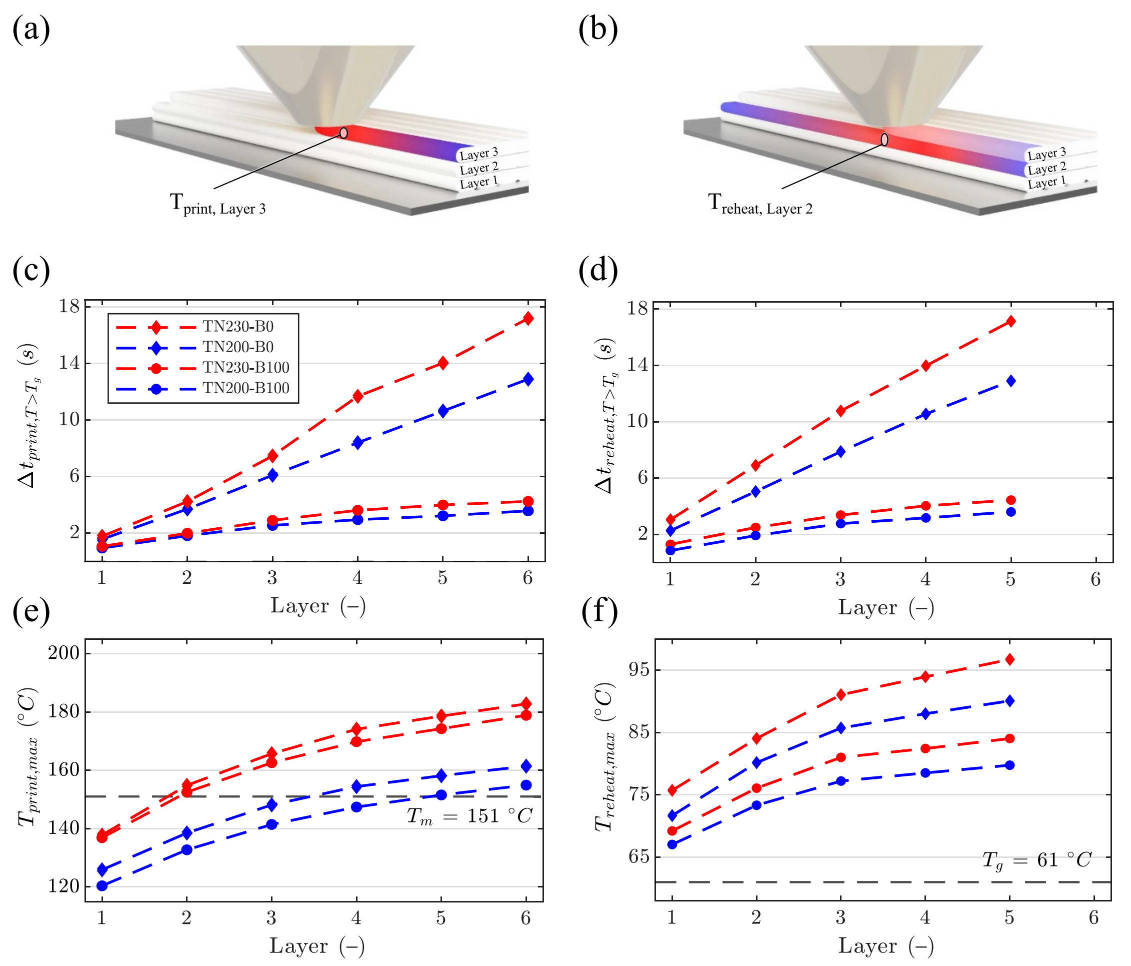

Figure 10. Thermal history of a multilayer structure during printing (v_p = 80 mm s^{-1}, Δt_inter = 20.58 s) as a function of layer; (a) visualization of cooling behavior during printing (b) visualization of reheating behavior of the underlying layer (c) cooling time above T_g (d) reheating time above T_g (e) extrusion temperature (f) maximum temperature recorded of the underlying line.

characteristics of the cooling curve for the parameter-dependent cooling of a 4D line is listed in the Supplementary material, see table S1.

$$T(t) = T_\mathrm{end} + (T_\mathrm{start} - T_\mathrm{end})\,\beta^t$$
$$T_\mathrm{start} = f(T_\mathrm{n}) \qquad \beta = f(B) \qquad T_\mathrm{end} = f(T_\mathrm{b})\,.$$

3.2. Thermal history of a 4D structure

This section analyses the thermal history of the multilayer 4D structure. Upon extrusion, the material starts cooling down, as discussed in the previous section 3.1. However, as long as the material temperature is above T_g, it exhibits increased molecular mobility, indicating an immediate start of stress relaxation. Stress relaxation is time- and temperature-dependent. Therefore, the maximum recorded temperature $T_\mathrm{print,max}$ and the cooling time $\Delta t_{\mathrm{print},T>T_\mathrm{g}}$ until the material temperature is below glass transition (T_g = 61° C) during printing are evaluated, see figure 10(a). When the layer is overprinted, its temperature increases due to heat transfer from the just extruded line. To consider implications for relaxation events, the maximum reheating temperature $T_\mathrm{reheat,max}$ and the duration above glass transition temperature $\Delta t_{\mathrm{reheat},T>T_\mathrm{g}}$ are recorded, see figure 10(b). Even though the temperatures are not direct predictors of stress relaxation, they are indicators of its dynamics.

Cooling time. Both the cooling time during printing as well as during reheating is strongly influenced by the part cooling fan B. For all specimens, the cooling time during printing $\Delta t_{\mathrm{print},T>T_\mathrm{g}}$ increases with number of deposited layers (figure 10(c)). The dominant influencing factors are the part cooling fan speed B and the nozzle temperature T_n, whereas the printing speed v_p shows only a minor effect, see figure S4 in the Supplementary material. Activation of the part cooling fan B significantly modifies the qualitative trend of $\Delta t_{\mathrm{print},T>T_{\mathrm{g}}}$. Printing with a deactivated part cooling fan ($B0$) causes a linear increase of $\Delta t_{\mathrm{print},T>T_{\mathrm{g}}}$ over the layers. In contrast, activating the part cooling fan ($B100$) limits the increase in $\Delta t_{\mathrm{print},T>T_{\mathrm{g}}}$, consequently indicating more homogeneous conditions across the structure's height. Increasing T_{n} does not change the qualitative trend but results in a systematic vertical shift toward higher $\Delta t_{\mathrm{print},T>T_{\mathrm{g}}}$ values, indicating generally slower cooling.

The qualitative trends of $\Delta t_{\mathrm{reheat},T>T_{\mathrm{g}}}$ are similar to those of $\Delta t_{\mathrm{print},T>T_{\mathrm{g}}}$ (figures 10(c) and (d)). $\Delta t_{\mathrm{reheat},T>T_{\mathrm{g}}}$ is predominantly affected by the part cooling fan speed B, while the nozzle temperature T_{n} has only a secondary effect.

Maximum temperature. The maximum temperature during printing $T_{\mathrm{print,max}}$ is significantly influenced by the nozzle temperature T_{n}, whereas the peak reheating temperature $T_{\mathrm{reheat,max}}$ is strongly affected by the part cooling fan speed B.

The maximum temperature during printing $T_{\mathrm{print,max}}$ corresponds to the investigated characteristic T_{start} in section 3.1. For all specimens, $T_{\mathrm{print,max}}$ increases with the number of deposited layers, indicating an increase of thermal energy within the structure. $T_{\mathrm{print,max}}$ is strongly influenced by the nozzle temperature T_{n}, while the part cooling fan speed B shows only minor effects. Higher printing speeds v_{p} result in generally lower $T_{\mathrm{print,max}}$ values. The qualitative trends observed for the printing parameters T_{n}, v_{p}, and B are consistent with the observations from the investigation of the cooling behavior of a single line.

The measured $T_{\mathrm{print,max}}$ values for the first layer are lower than the T_{start} values obtained in the single-line investigation. In some cases, the recorded values of $T_{\mathrm{print,max}}$ were even below the material's melting temperature T_m. This deviation is due to the limited resolution of the camera sensor. In the single-line investigation, the measurement fields covered the entire layer height h_{L}. In contrast, for the multilayer specimen, the measurement focused on the temperature of each layer. The measurement fields are set in the center of the layer to avoid measuring the temperature in the bonding zone between two layers. The measurement setup was kept consistent for all multilayer specimens. Despite the lower absolute temperature values, the qualitative trends remain consistent with those of the single-line investigation in section 3.1.

During the cooling of the upper line, the underlying line is reheated. $T_{\mathrm{reheat,max}}$ increases with the number of deposited layer. $T_{\mathrm{reheat,max}}$ consistently remains below the material's melting temperature ($T_m = 151^\circ$ C), implying that no remelting of the entire layer occurs, but only the layer boundaries fuse together. The part cooling fan speed B has a stronger influence on $T_{\mathrm{reheat,max}}$ than the nozzle temperature T_{n}. However, the overall qualitative trend of the temperature evolution remains almost unchanged by one of those two printing parameters.

The measurement data show that the thermal behavior of the underlying line is strongly affected by the part cooling fan speed B. When the fan is activated at $B100$, the heat introduced by the newly deposited line is dissipated to the environment by convection. In contrast, when the part cooling fan is deactivated ($B0$), convective heat transfer is significantly reduced, and more heat is transferred by conduction to the layer underneath. This shift in the heat transfer mechanism results in higher $T_{\mathrm{reheat,max}}$ values and a change in the trend of $\Delta t_{\mathrm{reheat},T>T_{\mathrm{g}}}$.

In addition, the data also indicate that the cooling time during printing, $\Delta t_{\mathrm{print},T>T_{\mathrm{g}}}$, decreases significantly when the part cooling fan B is activated. This observation is consistent with the findings from the single-line experiments, confirming the strong influence of convective heat transfer on the transient thermal behavior. However, this statement cannot be transferred to other 3D printers, as the fan's influence depends on the printing head design.

In conclusion, all parameters are clearly influenced by B and T_{n}. The part cooling fan speed B mainly influences the parameter $\Delta t_{\mathrm{print},T>T_{\mathrm{g}}}$ (figure 10(c)), $\Delta t_{\mathrm{reheat},T>T_{\mathrm{g}}}$ (figure 10(d)) and $T_{\mathrm{reheat,max}}$ (figure 10(f)) due to active cooling. The nozzle temperature T_{n} primarily affects $T_{\mathrm{print,max}}$ (figure 10(e)) by increasing the thermal energy of the extruded filament. In more general terms, the convective heat transfer can be improved by active cooling, resulting in faster cooling during printing and reduced reheating.

3.3. Shape change of a 4D structure

The activation process causes the 4D structure's shape change from the printed, temporary shape to the permanent shape, see figure 11(a). Shrinkage strain and curvature are the two characteristics that define the 4D structure after the shape change. The printing force-strain and printing force-curvature diagrams (figures 11(b) and (c)) divide the data points in four quadrants, which relate to the printing parameters T_{n} and v_{p}.

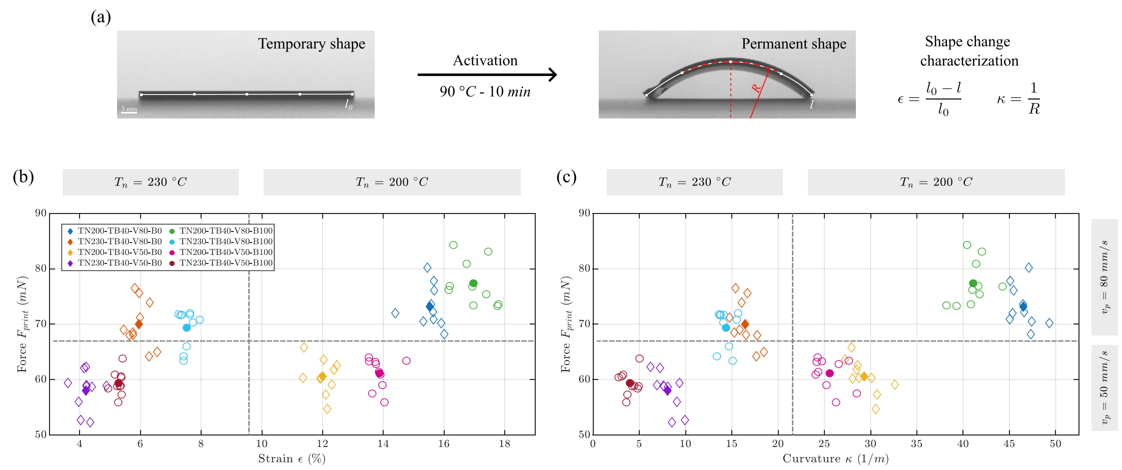

Figure 11. The experimental results show that the shape change is influenced by the investigated printing parameters. The shape change is quantified using the shrinkage strain ϵ and curvature κ (a). The activation of the part cooling fan increases the shrinkage strain (b). In contrast, the curvature is negatively influenced by the activation of the part cooling fan (c).

The printing parameters have a direct influence on the printing force F_{print} [28, 32]. For the printing parameters presented in figure 11 here, the printing speed v_{p} has the greatest influence on F_{print}, nozzle temperature T_{n} has a minor influence, while the influence of the part cooling fan B on the force is not determinable, which is consistent with Cerbe *et al* [28]. When increasing the printing speed by 30 mm s^{-1}, the printing force increases by approximately 10–17 mN. By increasing the nozzle temperature T_{n}, the printing force decreases. The relationship between the printing parameters and the printing force is consistent with previously published results [28, 32].

The activation results show more shrinkage for lower nozzle temperature T_{n}, higher printing speeds v_{p}, and an activated part cooling fan B (figure 11(b)). The average shrinkage ranges between 4.20% (TN230-TB40-V50-B0) and 16.97% (TN200-TB40-V80-B100). The nozzle temperature T_{n} has the greatest influence on the shrinkage. When T_{n} is increased by 30° C, the shrinkage reduces by approximately 8%–10%. Increasing the printing speed v_{p} from 50 to 80 mm s^{-1} increases shrinkage by 2%–4%. Activating the part cooling fan B has the smallest effect, causing a shrinkage increase of 1%–2%.

The average curvature ranges between 3.99m^{-1} (TN230-TB40-V50-B100) and 46.51m^{-1} (TN200-TB40-V80-B0) (figure 11(c)). Similar to the parameter-dependency of the shrinkage, the curvature increases with higher printing speeds v_{p} and lower nozzle temperatures T_{n}, indicating greater pre-strain inhomogeneity across the specimen's height. However, curvature is reduced by activating the part cooling fan B, indicating lower pre-strain inhomogeneity.

3.4. Discussion

It is observed that a similar printing force can lead to different shrinkages and curvatures (figure 11), which is consistent with the authors' previous study. The study implied that printing parameters modified the thermal history, leading to non-unique relationships between printing force and shrinkage. Although the printing force is a process-level indicator of the flow resistance of the directional printing process, it only implies a non-equilibrium state of the polymer chains. Similarly, the thermal measurement is a process metric and only implies the relaxation speed, i.e. the speed towards the equilibrium state. Section 3.2 showed that two events affect the layer temperature: deposition and overprinting. It also indicates that both events contribute to the relaxation of residual stress and lower the amount of recoverable shrinkage as discussed in section 3.2.

Printing parameters influence the shrinkage, indicating their influence on the residual stress state before activation. During printing, the material is strained inside the nozzle and at the nozzle outlet, resulting in a non-equilibrium state. The non-equilibrium state moves towards equilibrium due to relaxation. Below the glass transition temperature, the relaxation processes slow down considerably, freezing the current state. Therefore, the frozen-in non-equilibrium state below T_{g} is here referred to as residual stress σ_{res}.

The specimens' curvature is caused by greater shrinkage in the bottom layers than in the top layers. This also indicates higher residual stress in the bottom layers before activation (figure 12(a)). Notably, higher temperatures and longer thermal events were observed for the upper layers, indicating more

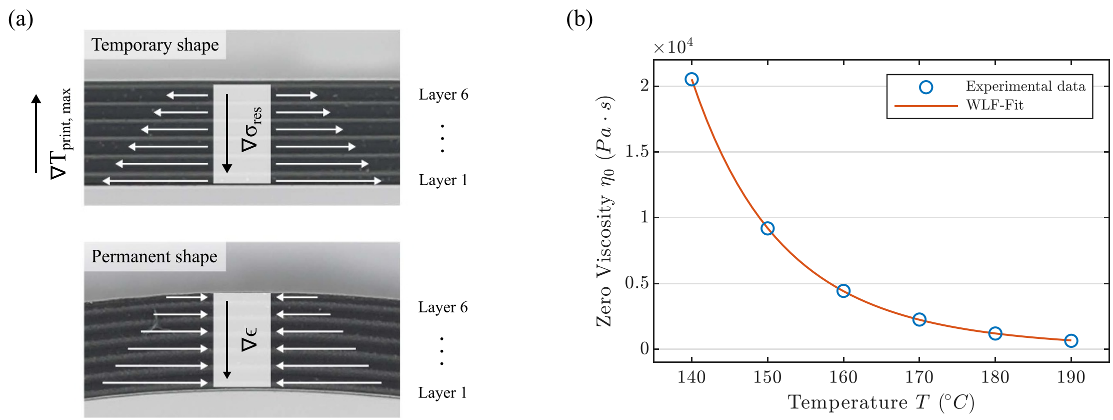

Figure 12. The stored pre-strain gradient correlates with the temperature gradient, causing different stress relaxation. (a) $T_{\text{print,max}}$, σ_{res}, ϵ gradient of a 4D structure in temporary shape before and permanent shape after activation. (b) Temperature-dependent zero viscosity η_0 of a Cross-WLF model with experimental and WLF-fit data, from [28]. The WLF-model fits the zero-shear viscosity data of PLA very well (RMSE $= 19.41$ Pa (s). Only zero viscosity is shown, as the material is no longer sheared after deposition. Stress relaxation time is approximately proportional to the zero viscosity.

Table 6. Cross-WLF model parameters for zero viscosity based on Cerbe *et al* [28]. Reproduced from [28]. CC BY 4.0.

Parameter	Value
Zero viscosity at the reference temperature D_1	2.0531×10^4 Pa · s
Reference temperature T_{ref}	$140°C$
1st WLF coefficient A_1	18.67
2nd WLF coefficient A_2	$222.8°C$

relaxation. Although the momentary non-equilibrium state directly after deposition remains unknown, the thermal history suggests that the specimens' curvature is relaxation-driven.

The part cooling fan has significant effects on the process that warrant discussion. First, its activation affects the thermal history by reducing the change in thermal events across layers, consequently indicating more homogenous relaxation. These results align with the reduction in curvature (κ), i.e. a lower gradient of shrinkage ($\nabla\varepsilon$). Second, its activation results in a small decrease in temperature immediately after deposition ($T_{\text{print,max}}$). While this effect is small compared to the other thermal history metrics, it still aligns with the increase in shrinkage observed during activation.

The thermal metrics imply a strong influence of the part cooling fan on taller structures. With an activated part cooling fan, all thermal metrics show decreasing gradients in the upper layers, approaching a limit value. Consequently, the thermal events are more homogeneous in the upper layers. However, if the part cooling fan is deactivated, the time above T_g increases linearly for deposition and reheating, indicating more inhomogeneous thermal events across layers. These effects are expected to increase with more layers. As a result, the part cooling fan is expected to have an even stronger influence on the layer-wise pre-strain gradient in thicker structures.

Although quantitative modeling is not the aim of this study, relaxation dynamics of PLA are discussed using a previously published Cross-WLF viscosity model [28]. Here, the model's temperature-dependent zero viscosity is used to estimate the change in relaxation dynamics with increasing temperature (equation (4) and table 6). The characteristic relaxation time of a simple viscoelastic Maxwell model is proportional to the zero viscosity (equation (5)),

$$\eta_0(T) = D_1 \cdot \exp\left(-\frac{A_1(T - T_{\text{ref}})}{A_2 + (T - T_{\text{ref}})}\right) \quad (4)$$

$$\tau \propto \eta_0(T). \quad (5)$$

The zero viscosity exponentially decreases with increasing temperature, see figure 12(b). Increasing the material temperature by 10° C reduces the zero viscosity by a factor of 2. This suggests a similar decrease in relaxation time, corresponding to a relaxation process twice as fast. In the context of 4D printing, this indicates that higher nozzle temperatures increase the relaxation speed, thereby decreasing the efficiency of storing the non-equilibrium state during the manufacturing process. The temperature measurements show that such high temperatures are reached only during deposition, not during overprinting. This indicates that relaxation during initial cooling dominates in this study.

4. Conclusion

This work advances the understanding of temperature-induced stress relaxation in FDM-based 4D printing by experimentally linking the thermal history during manufacturing to the shape change observed due to activation. The results demonstrate that printer design plays a critical role in heat transfer. In particular, the part-cooling fan governs convective heat transfer only within a limited spatial range, producing a distinct kink in the cooling curve, as shown in section 3.1. Furthermore, enhanced convective cooling reduces thermal history gradients in multilayer structures and thereby reduces inhomogeneous stress relaxation along the specimen height, as discussed in section 3.2. While increased convective cooling improves the predictability of shape change, its effect on inter- and intra-layer bond quality is yet to be determined for 4D structures. Overall, these findings emphasize the importance of controlled cooling strategies for predictable and reliable actuation in 4D-printed structures.

Within the scope of this study, stress relaxation during cooling was found to be more pronounced than relaxation induced by reheating during subsequent deposition. Although this is consistent in this study, the dominating effect changes with variations in the printer design, process parameters, or material. Previous studies have identified build plate temperature, material and surface roughness, printing speed, nozzle temperature, and interlayer delay time as influential parameters [15]. Building on these findings, this work demonstrates that the final stored pre-strain is governed by the combined effects of the initial pre-strain generated during extrusion, the thermal history, and the viscoelastic material properties. Consequently, any modification to printer design, process parameters, or material that alters polymer orientation, heat transfer, and thermal capacity, or viscoelastic relaxation directly influences both the magnitude of the stored pre-strain and its gradient along the specimen height.

The observed bending behavior provides a direct indication of the macroscopic gradient in layer-wise pre-strain. For smart structures printed with nominally identical process parameters, the resulting pre-strain gradient is attributed to the thermal history. Therefore, the thermal history can be used to increase relaxation in the lower or the upper layers, effectively tuning the pre-strain gradient to achieve convex, concave, or no bending responses. Importantly, these findings do not contradict the results reported by Bodaghi *et al* [15] and Noroozi *et al* [30], but rather provide direct experimental evidence of a thermally driven stress relaxation gradient underlying the observed bending behavior.

This work further identifies key design considerations for improving the controllability of FDM-based 4D printing. First, enhanced part cooling reduces pre-strain inhomogeneity by limiting the time the material remains above the glass-transition temperature T_g. Consequently, strong and spatially uniform cooling across the build plate is advantageous. Second, the build plate has a pronounced influence on the first layer, introducing a process-induced inhomogeneity. Creating thermal and surface conditions at the build plate that resemble those formed by printed layers can improve consistency in heat transfer and surface interaction. Third, inter- and intra-layer delay times exhibit a complex dependence on part geometry, printing speed, and toolpath.

There are three future directions derived from this study. First, complementary modeling and simulating the thermal history of 4D printing would improve our understanding and support the current experimental results with a theoretical basis. Second, effects that complicate the control of the thermal history, such as inter- and intra-layer delay times, could be addressed through software. It is thought that adapting slicing algorithms to incorporate controlled waiting times between layers and changing the print sequence of adjacent lines are promising approaches. Third, a future experimental study of the structural performance of 4D structures before and after activation could improve our understanding of interactions between shape change performance and bonding quality.

Acknowledgments

Funded by the Deutsche Forschungsgemeinschaft (DFG, German Research Foundation) - Project numbers 447858794; 498601949. The authors gratefully acknowledge the German Federal Ministry of Research, Technology, and Space (BMFTR) for supporting this work. Contributions of Project 498601949: Investigating the interlayer heat transfer. Contributions of Project 447858794: All other.

Data availability statement

The data that support the findings of this study are openly available at the following URL/DOI: https://doi.org/10.24355/dbbs.084-202601151221-0 [55].

Supplementary information available at https://doi.org/10.1088/1361-665X/ae7686/data1.

Author contributions

Philipp Herder 0009-0007-6954-9754
Data curation (equal), Formal analysis (equal), Investigation (equal), Validation (equal), Visualization (equal), Writing – original draft (equal)

Ferdinand Cerbe 0000-0002-6165-7378
Conceptualization (equal), Data curation (equal), Formal analysis (equal), Validation (equal), Visualization (equal), Writing – original draft (equal)

Michael Sinapius 0000-0002-1873-9140
Funding acquisition (lead), Resources (lead), Supervision (equal), Writing – review & editing (equal)

Christian Hühne 0000-0002-2218-1223
Funding acquisition (lead), Resources (supporting), Supervision (equal), Writing – review & editing (equal)

References

[1] Tibbits S 2014 *Archit. Des.* **84** 116–21
[2] Correa D 2022 *4D Printed Hygroscopic Programmable Material Architectures: Dissertation* (*Research Reports / Institute for Computational Design and Construction* vol 9 (Institute for Computational Design and Construction, University of Stuttgart)
[3] Mitkus R, Cerbe F and Sinapius ed M 2022 4d printing electro-induced shape memory polymers Smart Materials in Additive Manufacturing Volume 2 *Additive Manufacturing Materials and Technologies Ser* ed M Bodaghi and A Zolfagharian (Elsevier) pp 19–51
[4] van Manen T, Janbaz S and Zadpoor A A 2017 *Mater. Horiz.* **4** 1064–9
[5] Kačergis L, Mitkus R and Sinapius M 2019 *Smart Mater. Struct.* **28** 105042
[6] Deng Y, Zhang F, Jiang M, Liu Y, Yuan H and Leng J 2022 *ACS Appl. Mater. Interfaces* **14** 42568–77
[7] Hsu L Y, Mainik P, Münchinger A, Lindenthal S, Spratte T, Welle A, Zaumseil J, Selhuber-Unkel C, Wegener M and Blasco E 2023 *Adv. Mater. Technol.* **8**
[8] Wang F, Jiang M, Pan Y, Lu Y, Xu W and Zhou Y 2023 *Polym. Test.* **119** 107934
[9] Zolfagharian A, Jarrah H R and Bodaghi M 2021 *Bioprinting* **24** e00169
[10] Correa D, Papadopoulou A, Guberan C, Jhaveri N, Reichert S, Menges A and Tibbits S 2015 *3D Print. Addit. Manuf.* **2** 106–16
[11] Naficy S, Gately R, Gorkin R, Xin H and Spinks G M 2017 *Macromol. Mater. Eng.* **302** 1600212
[12] Simińska-Stanny J, Nizioł M, Szymczyk-Ziółkowska P, Brożyna M, Junka A, Shavandi A and Podstawczyk D 2022 *Addit. Manuf.* **49** 102506
[13] Chen A Y, Pegg E, Chen A, Jin Z and Gu G X 2021 *Adv. Intell. Syst.* **3**
[14] Ding A, Tang F and Alsberg E 2025 *Chem. Rev.* **125** 3663–771
[15] Bodaghi M, Damanpack A and Liao W 2017 *Mater. Des.* **135** 26–36
[16] Miao S, Zhu W, Castro N J, Nowicki M, Zhou X, Cui H, Fisher J P and Zhang L G 2016 *Sci. Rep.* **6** 27226
[17] Ouyang H, Li X, Lu X and Xia H 2022 *ACS Appl. Polym. Mater.* **4** 4035–46
[18] Wu W, Zhou Y, Liu Q, Ren L, Chen F, Fuh J Y H, Zheng A, Li X, Zhao J and Li G 2023 *Adv. Sci. (Weinh. Baden-Wurtt. Ger.)* **10** e2206486
[19] Caputo M P, Berkowitz A E, Armstrong A, Müllner P and Solomon C V 2018 *Addit. Manuf.* **21** 579–88
[20] Ge Q, Qi H J and Dunn M L 2013 *Appl. Phys. Lett.* **103** 131901
[21] Ge Q, Dunn C K, Qi H J and Dunn M L 2014 *Smart Mater. Struct.* **23** 094007
[22] Chapuis J N, Teufen G and Shea K 2025 *Smart Mater. Struct.* **34** 075034
[23] Schönfeld D, Chalissery D, Wenz F, Specht M, Eberl C and Pretsch T 2021 *Molecules* **26** 738–54
[24] Rahmatabadi D, Soltanmohammadi K, Aberoumand M, Soleyman E, Ghasemi I, Baniassadi M, Abrinia K, Bodaghi M and Baghani M 2024 *Phys. Scr.* **99** 025013
[25] Ali S J A, Rahmatabadi D, Baghani M and Baniassadi M 2024 *Macromol. Mater. Eng.* **309** 400069
[26] Galambos T, Temme K and Pretsch T 2026 *Smart Mater. Struct.* **35** 015041
[27] Mehrpouya M, Vahabi H, Janbaz S, Darafsheh A, Mazur T R and Ramakrishna S 2021 *Polymer* **230** 124080
[28] Cerbe F, González F A, Sinapius M, Behr M and Elgeti S 2026 *Addit. Manufact.* **118** 105108
[29] Hu G F, Damanpack A R, Bodaghi M and Liao W H 2017 *Smart Mater. Struct.* **26** 125023
[30] Noroozi R, Bodaghi M, Jafari H, Zolfagharian A and Fotouhi M 2020 *Polymers* **12** 519
[31] Cerbe F, Sinapius M and Böl M 2024 *Mater. Today: Proc.* **101** 1–6
[32] Cerbe F, Mahlstedt D, Sinapius M, Hühne C and Böl M 2024 *Prog. Addit. Manufact.* **9** 123–32
[33] Bodaghi M, Noroozi R, Zolfagharian A, Fotouhi M and Norouzi S 2019 *Materials* 12

[34] Noroozi R, Zolfagharian A, Fotouhi M and Bodaghi M 2022 4d-printed shape memory polymer: Modeling and fabrication *Smart Materials in Additive Manufacturing Volume 2 Additive Manufacturing Materials and Technologies Ser* ed M Bodaghi and A Zolfagharian (Elsevier) pp 195–228

[35] Alshebly Y S and Nafea M 2023 *Smart Mater. Struct.* **32** 064008

[36] An B *et al* 2018 Thermorph: Democratizing 4d printing of self-folding materials and interfaces *Proc. 2018 CHI Conf. on Human Factors in Computing Systems* (*New York, NY, USA*) edR Mandryk, M Hancock, M Perry and A Cox (ACM)) pp 1–12

[37] de Gennes P G 1971 *J. Chem. Phys.* **55** 572–9

[38] Doi M and Edwards S F 1978 *J. Chem. Soc., Faraday Trans* **74** 1789–801

[39] Williams M L, Landel R F and Ferry J D 1955 *J. Am. Chem. Soc.* **77** 3701–7

[40] Compton B G, Post B K, Duty C E, Love L and Kunc V 2017 *Addit. Manuf.* **17** 77–86

[41] Vanaei H R, Raissi K, Deligant M, Shirinbayan M, Fitoussi J, Khelladi S and Tcharkhtchi A 2020 *J. Mater. Sci.* **55** 14677–89

[42] Hossain R E N, Lewis J and Moore A L 2021 *Addit. Manuf.* **47** 102328

[43] Caltanissetta F, Dreifus G, Hart A J and Colosimo B M 2022 *Addit. Manuf.* **58** 102995

[44] Sadaf A I, Ahmed H and Khan M R 2024 *Int. J. Adv. Manuf. Technol.* **134** 5631–42

[45] Ferraris E, Zhang J and Hooreweder B 2019 *CIRP Ann.* **68** 213–6

[46] Wolszczak P, Lygas K, Paszko M and Wach R A 2018 *Rapid Prototyp. J.* **24** 615–22

[47] Kousiatza C, Chatzidai N and Karalekas D 2017 *Sensors* **17** 456

[48] Zhang J, Winkel J, Gatarek D, Sel K, Geyskens K, Hooreweder B and Ferraris E 2025 *Appl. Therm. Eng.* **280** 128217

[49] Prajapati H, Salvi S S, Ravoori D and Jain A 2020 *Polym. Test.* **92** 106866

[50] Usamentiaga R, Venegas P, Guerediaga J, Vega L, Molleda J and Bulnes F G 2014 *Sensors* **14** 12305–48

[51] Lee C Y and Liu C Y 2019 *Addit. Manuf.* **25** 196–203

[52] Lambiase F and Pace F Andreucci E and Paoletti A 2024 *Int. J. Adv. Manuf. Technol.* **133** 1–11

[53] Wijnen B, Sanders P and Pearce J M 2018 *Prog. Addit. Manuf.* **3** 193–203

[54] Santos T, Gaspar M, Amaral J, Amaral V, Ferreira N, Alves N and Pascoal-Faria P 2023 *J. Manuf. Mater. Process.* **7** 189

[55] Herder P, Cerbe F, Sinapius M and Hühne C 2026 Experimental investigation of the thermal history in FDM-based 4D printing *LeoPARD – TU Braunschweig Publications And Research Data* (https://doi.org/10.24355/dbbs.084-202601151221-0)